Characterization of Iron-Rich Phyllosilicates Formed at Different Fe/Si Ratios

Liva Dzene, Patrick Dutournie, Jocelyne Brendle, Lionel Limousy, Jean-Marc Le Meins, Laure Michelin, Loïc Vidal, Simon Gree, Mustapha Abdelmoula, Christelle Martin, et al.

CHARACTERIZATION OF IRON-RICH PHYLLOSILICATES FORMED AT DIFFERENT Fe/Si RATIOS

Liva Dzene[a,*], Patrick Dutournie[a], Jocelyne Brendle[a], Lionel Limousy[a], Jean-Marc Le Meins[a], Laure Michelin[a], Loïc Vidal[a], Simon Gree[a], Mustapha Abdelmoula[b], Christelle Martin[c], and Nicolas Michau[c]

[a]Institut de Science des Matériaux de Mulhouse CNRS UMR 7361, Université de Haute-Alsace, Université de Strasbourg, 3b rue Alfred Werner, 68093 Mulhouse CEDEX, France

[b]LCPME, CNRS-Université de Lorraine UMR7564, Nancy, F-54000, France

[c]Andra, R&D Division, Packages and Materials Department, 1/7 rue Jean Monnet, F-92298 Châtenay-Malabry CEDEX, France

*liva.dzene@uha.fr

Abstract–The formation of 2:1 and 1:1 phyllosilicates in Fe–Si–O–H systems occurs in various geological and engineering settings; however, the identification and characterization of these minerals is very challenging due to a limited amount that is accessible, the very small particle size, and often very high heterogeneity of these samples. To overcome these drawbacks, the synthesis of iron-rich phyllosilicates was attempted in this study with an initial Fe/Si molar ratio ranging from 0.50 to 2.33. The synthesis was performed at 150°C under hydrothermal conditions during 7 days. Synthesis products were characterized by X-ray diffraction and fluorescence, by infrared, Raman, and Mössbauer spectroscopies, and transmission electron microscopy. Results revealed that the stability field of the 2:1 clay mineral was wider than that of the 1:1 clay mineral. The 2:1 clay mineral was less sensitive to redox conditions compared to the 1:1 clay mineral. In addition, a heterogeneity of formed phases (iron oxides, nontronite, cronstedtite, or greenalite) was identified.

Keywords–Berthierine, Cronstedtite, Greenalite, Nontronite, Serpentine, Synthesis

INTRODUCTION

The formation of phyllosilicates in the Fe–Si–O–H system has been reported in various geological and engineering settings: on meteorites (Elmaleh et al., 2015; Lauretta et al., 2000; Muller et al., 1979; Zolensky et al., 1993; Zolotov, 2014), on Mars (Bishop et al., 2008; Ehlmann et al., 2011), in deep-sea sediments (Badaut et al., 1985, 1992; Baldermann et al., 2015; Marcus & Lam, 2014), in iron-banded formations (Eugster & Chou, 1973; Grubb, 1971), in ore deposits (Inoué & Kogure, 2016; Rasmussen et al., 1998; Rivas-Sanchez et al., 2006), at iron-clay (Lanson et al., 2012; Le Pape et al., 2015; Pignatelli et al., 2014) and steel-glass interfaces (Carriere et al., 2017, 2021; Schlegel et al., 2016), and as a scale deposit in brine-handling equipment (Manceau et al., 1995). Thermodynamic modeling for some of these settings has been performed with the intention of estimating the physicochemical conditions which led to the formation of these minerals in the past (Chevrier et al., 2007; Fritz & Toth, 1997; Zolotov, 2014), or of estimating the evolution of physicochemical conditions for a given mineralogical composition with time (Ngo et al., 2015; Wilson et al., 2015).

The incorporation of iron-rich phyllosilicates in such models is challenging for several reasons. First, for some settings such as iron–glass interfaces, the identification of newly-formed minerals is rather arduous due to their very small particle size. The thickness of the alteration layer between iron and glass is in the range of 1 µm (Carriere et al., 2017, 2021; Schlegel et al., 2016). Second, the information regarding experimentally measured thermodynamic properties of iron-rich minerals is very limited. Such data are available only for nontronite (Gailhanou et al., 2013) and greenalite (Tosca et al., 2016). Last, the minerals such as cronstedtite, hisingerite, berthierine, brindleyite, minnesotaite, and saponite are not widely abundant and not readily accessible for experiments. Given the lack of accessible material for experiments, an alternative approach is to infer the physicochemical properties by estimating the thermodynamic constants using various methods such as the summation of the properties of respective oxides (Tardy & Garrels, 1974) or the decomposition into polyhedral units (Blanc et al., 2015). However, these approaches do not take into account such aspects as polytypism or cation substitution. The study of Pignatelli et al. (2014) discussed the mismatch between geochemical modelling results and experimental observations for $T < 50$°C, and attributed the discrepancy to the presence of different cronstedtite polytypes. Shulte & Shock (2004) considered the difference of stability between greenalite and cronstedtite. The presence of ferric iron in tetrahedral coordination in cronstedtite might be the reason for the smaller stability field for cronstedtite (up to 100°C) compared to the one of greenalite (up to 150°C).

Indeed, the characterization of mineral composition of the different settings often reveal the coexistence of several phyllosilicates (Badaut et al., 1992; Ehlmann et al., 2011; Elmaleh et al., 2015; Evans et al., 2017; Lanson et al., 2012; Lauretta et al., 2000; Le Pape et al., 2015; Marcus & Lam, 2014; Pignatelli et al., 2014; Tutolo et al., 2019). Furthermore, for the same type of phyllosilicate mineral, the basic structure can be heterogeneous in terms of different types of layers (Chukhrov et al., 1979; Inoué & Kogure, 2016; Suquet et al., 1987), iron distribution between octahedral and tetrahedral sheets (Gates et al., 2002; Stucki, 2013), as well as the distribution of iron within the octahedral sheet (Vantelon et al., 2003). Thus, Chukhrov et al. (1979) reported ferric phyrophillite exposed to glycol and ethylene glycol having different types of layers (swelling vs non-swelling) suggesting a heterogeneous structure. Similarly, Suquet et al. (1987) studied nontronite swelling and observed a continuous evolution of layer-to-layer distance as a function of relative humidity with no clearly distinguishable steps. Step-like behavior is characteristic of crystalline, homogeneous phyllosilicates suggesting that the studied nontronite samples might have a rather complex structure. A detailed study of chlorite with HRTEM by Inoué & Kogure (2016) also revealed a complex stacking structure of two different types of layers: berthierine and chlorite. In another study, Gates et al. (2002) explored the coordination of iron (tetrahedral vs octahedral) in various natural nontronite samples and reported different distributions between tetrahedral and octahedral iron in various samples. Finally, Vantelon et al. (2003) studied the distribution of iron in the octahedral sheet of different dioctahedral smectites and found three distinct groups: the first with an ordered distribution, the second with a random distribution, and the third group had clusters of iron.

The examples reported above illustrate the complexity of phyllosilicates at different levels: different mineral phases, different types of layers within one mineral, and different distributions of iron between and within sheets composing the layers. How can one address this complexity and obtain enough relevant material for experiments for the measurements of physicochemical properties of iron-rich phyllosilicates? A solution to this issue is to synthesize such materials in laboratory conditions. Moreover, the conditions of such a synthesis should be as close as possible to the studied system. This would enable the necessary quantities of phyllosilicates for detailed characterization of their properties and further experiments to be obtained.

The formation of phyllosilicates in the Fe–Si–O–H system has been reported previously under reducing (Farmer et al., 1991; Flaschen & Osborn, 1957; Francisco et al., 2020; Harder, 1976; Hinz et al., 2021; Mizutani et al., 1991; Pignatelli et al., 2020; Tosca et al., 2016) and oxidizing (Baron et al., 2016; Decarreau et al., 1987; Decarreau et al., 2008; Roy & Roy, 1954) conditions

at neutral to basic pH and at different temperatures (from 23 to 470°C) and synthesis durations (4 days to 3 months). In the experiments with Fe/Si initial molar ratio 0.75 or lower, the formation of nontronites was independent of the atmospheric conditions. The composition of the precipitated solid with respect to Fe/Si molar ratio is always higher than the initial Fe/Si molar ratio. The study of Baron et al. (2016) showed that this ratio depended on the pH of the solution, which in turn determined the speciation of Si in the solution. For the initial Fe/Si molar ratio higher than 0.75, the formation of 1:1 phyllosilicates was reported except in the study of Mizutani et al. (1991), where they observed the formation of 2:1 phyllosilicate at initial Fe/Si = 1.50. Thus, the predominance of one or the other kind of phyllosilicate depends not only on the physicochemical conditions (i.e. thermodynamics) but also on the respective formation kinetics, influenced by the temperature (activation energy). This conclusion is in agreement with the conclusions reached in a previous study (Boumaiza et al., 2020), in which the kinetics of 2:1 clay mineral formation was faster than for 1:1 clay mineral formation. Thus, the experiment at higher temperature would have faster kinetics and favor the formation of 2:1 phyllosilicates. Indeed, the experiment of Mizutani et al. (1991) was performed at 150°C. In comparison, the experiment of Tosca et al. (2016) performed at room temperature reported the precipitation of greenalite (1:1 phyllosilicate) at initial Fe/Si = 0.8.

These previous results show that the initial Fe/Si molar ratio influences the type of phyllosilicate formed. Therefore, the aim of the current study was to investigate the effect of a wider range of Fe/Si molar ratio (0.50 to 2.33) on the formation of phyllosilicates. The synthesis of the products was performed at hydrothermal conditions in order to maximize the yield and crystallinity of the products (Decarreau et al., 2008).

EXPERIMENTAL

Synthesis of Materials

Iron(II) sulfate ($FeSO_4 \cdot 7H_2O$, purity of 99.5%; Sigma Aldrich, India) was dissolved in 70 mL of deionized water (18.2 MΩ·cm), then 0.041 g (0.5 wt.%) of sodium dithionite ($Na_2S_2O_4$, purity of 85%; Alfa Aesar, Kandel, Germany) was added to the solution to limit Fe^{2+} oxidation. Next, a certain amount of sodium orthosilicate (Na_4SiO_4; Alfa Aesar, Karlsruhe, Germany) was added to the Fe(II) solution; the quantities of Fe(II) sulfate and sodium orthosilicate were calculated assuming a theoretical yield of 2 g of phyllosilicate with initial Fe/Si molar ratios ($(Fe/Si)_{ini}$) ranging from 0.50 to 2.33 (Table 1). The amount of reactants used in the synthesis for each sample is reported in Supplementary Information Table S1. The suspension was

homogenized for 2 h by stirring at 200 rpm. The pH was then measured in an aliquot withdrawn from this initial suspension (pH_{ini}) and then again in an aliquot of the supernatant withdrawn after the synthesis (pH_f) using a combination pH electrode (HANNA Instruments, Nusfalau, Romania) that was calibrated at 20°C before the measurements using two pH buffer solutions (pH = 7.00 and pH = 10.00). Preliminary tests with standard solutions revealed that the probe gave accurate measurements until pH = 13.60. The redox potential was measured after 2 h of stirring (Eh_{ini}) in an aliquot withdrawn from the suspension and in the aliquot of the supernatant after the synthesis (Eh_f) using a combination redox electrode (HANNA Instruments, Nusfalau, Romania). The redox probe was calibrated with a standard solution of +200.00 mV (ORP buffer solution, Hach, Loveland, USA) before the measurements. The reported values were recalculated with respect to potential of the standard hydrogen electrode.

Table 1. Initial Fe/Si molar ratios and solution characteristics before and after the synthesis. $(Fe/Si)_{solid}$ molar ratio after the synthesis was calculated using XRF results

Before synthesis			After synthesis		
$(Fe/Si)_{ini}$ molar	$pH_{ini.}$	Eh_{ini} (mV/SHE)	$(Fe/Si)_{solid}$ molar	pH_f	Eh_f (mV/SHE)
2.33	7.36	-481	5.40	4.73	355
1.50	12.64	-375	2.99	12.81	36
1.00	13.22	-576	1.47	13.41	24
0.75	13.33	-592	1.41	13.41	155
0.50	13.60	-624	1.46	13.61	80

The synthesis was performed in 150 mL Teflon-lined stainless-steel mineralization bombs (Ref.: 2148.6000, Top Industry®, Vaux-le-Pénil, France) at 150°C for 7 days, the pressure corresponded to the saturation pressure at 150°C. After 7 days, the autoclaves were removed from the oven and left to cool down. The samples were removed from the autoclaves and washed with deionized water 3 times by centrifugation at 10,000 rpm (12,860×*g*) for 10 min.

Characterization Methods

Powder X-ray diffraction. Data were collected with a powder diffractometer D8 ADVANCE A25 from Bruker (Karlsruhe, Germany) in Bragg-Brentano reflexion geometry θ–θ (goniometer radius 280 mm). This diffractometer was equipped with the LynxEye XE-T high resolution energy dispersive 1-D detector ($CuK\alpha_{1,2}$), leading to ultra-fast X-ray diffraction

measurements. A motorized anti-scatter screen was used for effective suppression of instrument background, most importantly air-scatter at low angles. Optical components were limited to two Soller slits (2.5°) for primary and secondary optics, and motorized divergence slits. Conditions for data collection were the following: angular area 3–70°2θ, step size 0.017°2θ, time per step 1.8 s (total time per step was 345 s), variable divergence slits mode (irradiated sample length 15 mm), total time for acquisition 2 h. During data collection, powder samples were rotated at 5 rpm. All the data were converted and presented into fixed divergence slits mode.

After the identification of phyllosilicates by powder X-ray diffraction, three samples with $(Fe/Si)_{ini}$ = 1.00, 0.75, and 0.50 containing 2:1 phyllosilicates were saturated with Ca^{2+} using 1 M $CaCl_2$ (≥99.0%, Sigma Aldrich, Steinheim, Germany) solution (Bergaya & Lagaly, 2013) to limit a possible impact of relative humidity conditions during the characterization. After washing, the samples were dried at 40°C, ground by hand in a mortar, and stored in glass vials at room conditions. To differentiate between chlorite and swelling 2:1 phyllosilicates, these three samples were exchanged with 1 M CH_3COONH_4 (>98%, Emsure, Darmstadt, Germany) for 24 h.

X-ray diffraction of oriented preparations. To discriminate between swelling/non-swelling phyllosilicates, orientated preparations were made by dispersing synthesis products in ~1 mL distilled water. Oriented preparations allow enhancement of 00*l* reflections characteristic for layered minerals. Saturation with ethylene glycol was performed by exposing oriented slides to an ethylene glycol saturated atmosphere in a desiccator for 2 days. Samples were recorded immediately after the removal from the desiccator from 2 to 15°2θ angular range on an X'Pert Pro from PANalytical (Almelo, The Netherlands) equipped with an X'Celerator real-time multiple strip detector operating with an angular aperture of 2.12°2θ using CuKα radiation with a wavelength of 0.15418 nm. Diffractograms were recorded at room temperature with a step size of 0.017°2θ and a scan time of 4 s per step (total time per step was 220 s). The divergence slit, the anti-scatter slit, and the two Soller slits were 0.0625°, 0.125°, and 2.3°, respectively. To ensure that the sample did not evolve during the recording, the diffraction pattern was recorded twice for some samples. As no change was observed between the two recordings, it was concluded that during the recording time the sample remained stable.

X-ray fluorescence. The Fe/Si ratio in synthesis products was determined by X-Ray fluorescence with a PANalytical (Almelo, The Netherlands) Zetium spectrometer. Dry samples of 200 mg were pressed into 13 mm diameter pellets by applying a pressure of 4 T for 5 min.

Infrared spectroscopy. The FTIR spectra were recorded using a Bruker Equinox 55 FTIR spectrometer (Karlsruhe, Germany) equipped with a DTGS detector in transmission mode. The spectra were recorded in the mid-infrared region (MIR) from 4000 to 400 cm^{-1} with a resolution of 4 cm^{-1}. Samples were prepared in the form of KBr pellets obtained by mixing 1 mg of sample with 100 mg of KBr, pressed, and dried at 120ºC.

Mössbauer spectroscopy. Mössbauer spectroscopy was performed at 290, 77, 15, and 4 K with a constant acceleration device. The Mössbauer spectrometer was equipped with a 512 multichannel analyzer (Halder Electronic Gmbh, Seehausen, Germany) and a 50 mCi source of ^{57}Co in a Rh matrix. Data were obtained from appropriate amounts (10 mg of Fe per cm^2) of solid samples to get optimal experimental conditions. In order to avoid the condensation of oxygen and water on the walls of the cryostat, samples were transferred rapidly under an inert He atmosphere to a cold-head cryostat, equipped with a vibration isolation stand and developed in the LCPME Laboratory. The recordings at 290, 77, and 15 K were performed on a spectrometer equipped with the Advanced Research Systems cryostat (model DE-204SF), while the recordings at 4 K were done on the spectrometer coupled to the Janis Cryostat (model SHI-850-5). Both cryostats operate in a closed cycle on the principle of the Gifford-Mc Mahon refrigeration. Mössbauer spectra were collected in transmission mode. The 50 mCi source of ^{57}Co in a Rh matrix was maintained at room temperature (RT) and mounted at the end of a Mössbauer velocity transducer. The spectrometer was calibrated with a 25 μm foil of α-Fe at RT. Analysis of the Mössbauer spectra consisted of least-squares fitting of data with a combination of two-peak quadrupole components (doublets) and, when present, six-peak magnetic hyperfine components (sextets). The Voigt-based fitting method of Rancourt & Ping (1991) for quadrupole splitting distribution (QSDs) and magnetic hyperfine fields (HFDs) was used to fit spectra.

Transmission electron microscopy coupled with energy dispersive X-ray spectroscopy. For the observations under transmission electron microscopy (TEM), a few particles of sample were dispersed in chloroform using ultrasound and deposited on a 300-mesh copper TEM grid. Images were acquired using an ARM200 field emission transmission electron microscope (JEOL, Tokyo, Japan) equipped with an ultra-high resolution pole-piece operating at 200 kV. The TEM images were analyzed using *Digital Micrograph* software. Chemical analysis of selected zones was performed using energy dispersive X-ray spectroscopy. The reported semi-quantitative values of the chemical compositions (or ratios) were the mean of 5 measurements.

Raman spectroscopy. Raman spectra were obtained with a Horiba LABRAM 300 confocal-Raman spectrometer (Lille, France) equipped with a Compass 315M-50 laser (50 mW, 532 nm), diffraction gratings of 600 grooves mm^{-1} and a CCD matrix detector. Laser focusing and sample viewing were performed through an Olympus BX40 microscope fitted with ×50 objective lens. The spot size was ~15–20 µm with a resolution of 4 cm^{-1}. Laser power could be reduced by filters to ~1, 0.1, and 0.01 mW.

RESULTS

Mineralogical and Chemical Composition of Synthesis Products

Crystalline phase analysis of synthesis products showed that for $(Fe/Si)_{ini} \leq 1.00$, 2:1 phyllosilicate was formed (Fig. 1). The 2:1 phyllosilicate was identified in XRD by its characteristic reflections at 6.26; ~19.20–19.30; ~34.00, and 60.06°2θ (i.e. 14.11, 4.62–4.58, 2.60, and 1.54 Å, respectively) (Brindley & Brown, 1982). Calcite ($CaCO_3$) was also present as an impurity. This could be due to the use of dithionite, in which calcite was used as a stabilizer; or it may have been the result of precipitation of carbonate upon the sample saturation with calcium during post-synthesis treatment. For $(Fe/Si)_{ini} > 1.00$, a 1:1 phyllosilicate was identified (Fig. 1) based on characteristic reflections at 12.36, 24.91, 35.01, 41.33, 50.84, 58.21, and 59.56°2θ (i.e. 7.16, 3.57, 2.56, 2.19, 1.79, 1.59, and 1.55 Å, respectively) (Bailey, 1988; Hybler, 2006). For the sample with $(Fe/Si)_{ini} = 1.50$, thenardite (Na_2SO_4) was identified, due to the use of dithionite and sulfate as anions during the synthesis. For samples with $(Fe/Si)_{ini} = 2.33$, various iron oxide phases were identified.

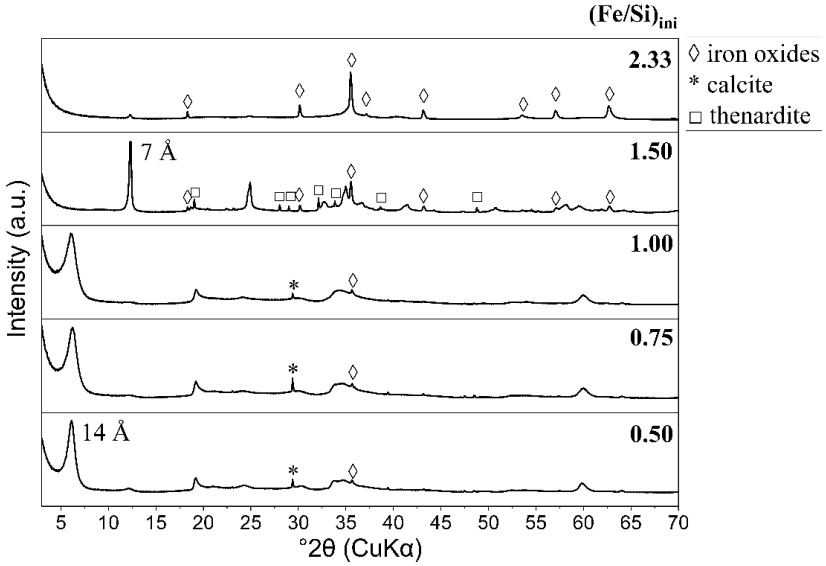

Fig. 1. Powder X-ray diffractograms of synthesis products for $0.50 \leq (Fe/Si)_{ini} \leq 2.33$

Analysis by XRF of synthesis products showed that the (Fe/Si) molar ratio after the synthesis was higher than the (Fe/Si) molar ratio introduced in the mixture, suggesting only partial iron-rich phyllosilicate precipitation and the formation of other Fe-bearing phases (Table 1). This is in agreement with the identified crystalline phases. For the sample with the initial Fe/Si = 2.33, the pH dropped significantly upon precipitation and after synthesis due to the hydrolysis and condensation of iron and silicon into various solid phases (Eqs 1 and 2).

$$Fe^{2+} + 2\ H_2O \rightarrow Fe(OH)_2 + 2\ H^+ \quad (1)$$

$$Fe^{3+} + 3\ H_2O \rightarrow Fe(OH)_3 + 3\ H^+ \quad (2)$$

The solubility of silica is lower in acidic pH compared to basic pH (Iler, 1979). It could thus explain the absence of phyllosilicates and the presence of various iron oxides identified only by XRD. Magnetite was identified in the sample with $(Fe/Si)_{ini}$ = 1.50 and hematite in samples with $(Fe/Si)_{ini} \leq 1.00$. Although the system was in reducing conditions upon precipitation (negative Eh), after synthesis it clearly became oxidizing (close to zero or positive Eh) (Table 1).

Characterization of 1:1 Phyllosilicate Containing Synthesis Product

The sample with $(Fe/Si)_{ini}$ = 1.50 was chosen for a more detailed characterization as it indicated a superior phyllosilicate phase crystallinity compared to the sample with $(Fe/Si)_{ini}$ = 2.33 (Fig. 1). Infrared spectroscopy showed O-H and Si-O bond stretching and bending vibrations (Fig. 2 and Table 2). Sharp peaks at 1194, 1109, and 619 cm^{-1} correspond to thenardite, which was also identified by pXRD (Farmer, 1974). The 620 cm^{-1} band could be a combination of O–H deformation and Fe(III)–O_{apical} stretching vibrations (Neumann et al., 2011). Previous studies reported that the presence of Fe(II) in phyllosilicate makes the spectra featureless (Fialips et al., 2002; Manceau et al., 2000), suggesting that some of the iron might have been incorporated as Fe(II). It has to be noted that the intensity and position of bands can be affected by sample orientation, and polytypic sequence. Two low-intensity bands at 1634 and 1400 cm^{-1} correspond to vibrations of water molecules and carbonate anions, respectively.

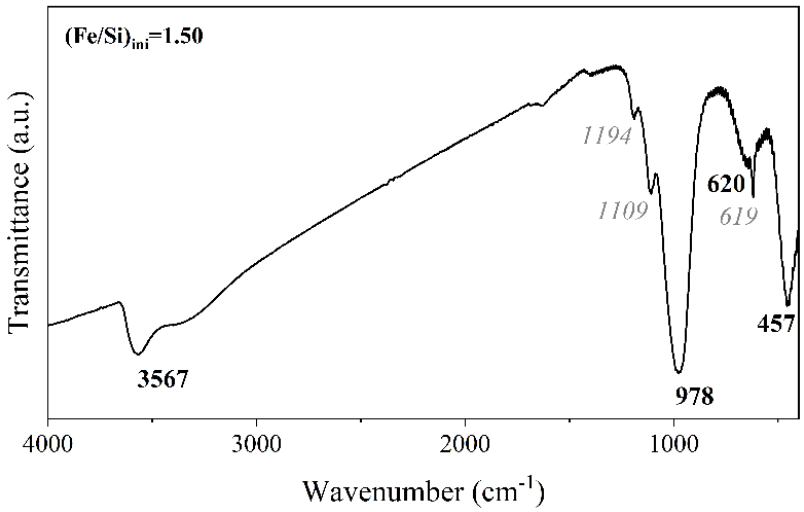

Fig. 2. FTIR spectrum of $(Fe/Si)_{ini}$ = 1.50 synthesis product

Table 2. Identified FTIR bands and corresponding vibration modes for $(Fe/Si)_{ini}$ = 1.50

Wavenumber (cm^{-1})	Vibration mode
3567	O–H stretching
978	Si–O stretching
620	O–H bending / Fe(III)–O_{ap} stretching
457	Si–O bending

To explore if Fe(II) was present in the sample as suggested by FTIR, further analysis using Mössbauer spectroscopy was performed. The Mössbauer spectrum at 77 K was chosen to be presented and discussed here, as at this temperature iron oxides can be differentiated from phyllosilicates. Often, the recording spectra at 4 K is considered as a true diagnostic for the presence of most minerals. However, in the case of polymineralic samples at very low temperature, to discern the presence of magnetite and its multiple sextets might be challenging due to the overlap of the magnetite sextets with other phases (e.g. spectra at 15 and 4 K in Figs S1 and S2 in Supplementary Information). Exploiting the spectrum at 77 K is more convincing, even if the magnetically ordered phase was much less abundant than the paramagnetic component. The spectrum at room temperature showed just a few traces of the magnetically ordered phase in the background noise (Fig. S1 in Supplementary Information). This component was more enhanced at 77 K due to the temperature effect. The spectrum of

277 $(Fe/Si)_{ini}$ = 1.50 sample obtained at 77 K clearly confirmed the presence of Fe(II) as two
278 doublets with chemical shift of 1.21 and 1.39 mm/s (Fig. 3 and Table 3) (Murad, 2006).

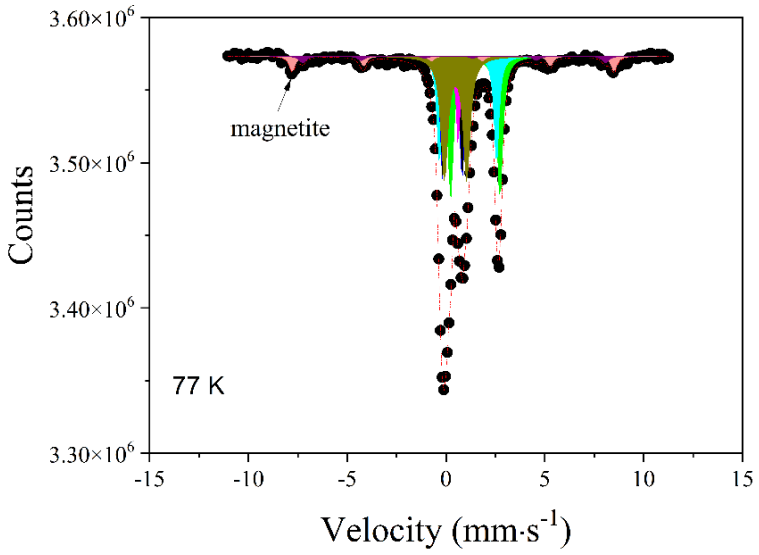

279

280 **Fig. 3.** Mössbauer spectrum for synthesis product with $(Fe/Si)_{ini}$ = 1.50 at 77 K

281 In total, five doublets and two sextets were necessary to describe the experimentally obtained
282 spectra (Table 3). The two sextets corresponded to magnetite (Stucki, 2013), which was
283 identified also by pXRD. It is generally agreed that below the Vervey temperature the magnetite
284 spectrum is fitted with 5 sextets (Vandenberghe et al., 2000). In the current case, given the
285 abundance of the magnetically ordered component, it seemed misleading to fit the spectrum
286 part corresponding to magnetite with 5 components as indicated in the literature. It seemed
287 more convincing to fit with only two sextets of most abundant components instead. Three
288 doublets with center shifts of 0.26, 0.33, and 0.54 mm/s were attributed to Fe(III). Two doublets
289 with center shifts of 0.33 and 0.26 mm/s corresponded to octahedrally and probably
290 tetrahedrally coordinated Fe(III) of 1:1 phyllosilicate, respectively (Baron et al., 2017). The
291 third doublet of Fe(III) with center shift of 0.54 mm/s could be attributed to amorphous or
292 poorly crystalline iron oxides not revealed by pXRD. Finally, the two doublets with large values
293 of center shifts of 1.21 and 1.39 mm/s corresponded to Fe(II) of 1:1 phyllosilicate (Chemtob et
294 al., 2015). Mössbauer spectroscopy revealed the high complexity of the sample having several
295 mineral phases: phyllosilicates, magnetite, and poorly crystallized iron oxide.

296

297 **Table 3**. Mössbauer parameters for synthesis product with $(Fe/Si)_{ini}$ = 1.50 at 77 K, where CS
298 is center shift, Δ is quadrupole splitting, H is hyperfine field, and R.A. is relative abundance

	CS (mm/s)	Δ (mm/s)	H (kOe)	R.A. (%)	
Doublet (1)	1.39	2.33		21	Fe(II) in clay mineral
Doublet (2)	1.21	3.05		20	Fe(II) in clay mineral
Doublet (3)	0.33	0.96		16	Fe(III) octahedral clay
Doublet (4)	0.26	0.66		9	Fe(III) tetrahedral clay
Doublet (5)	0.54	0.99		26	Fe(III) poorly cryst. iron oxides
Sextet (6)	0.45	-0.09	505	5	Magnetite
Sextet (7)	0.27	0.13	475	3	Magnetite

299

300 Considering the complex mineralogy of the sample, an observation of particles under
301 transmission electron microscopy (TEM) was carried out to learn more in detail about the
302 structure and chemistry of phyllosilicates only. Observations by TEM revealed the layer
303 structure characteristics of 1:1 phyllosilicates with an average layer-to-layer distance of 7 Å
304 (Fig. 4). Different thicknessed of particles was observed, ranging from a few layers to several
305 tens of layers.

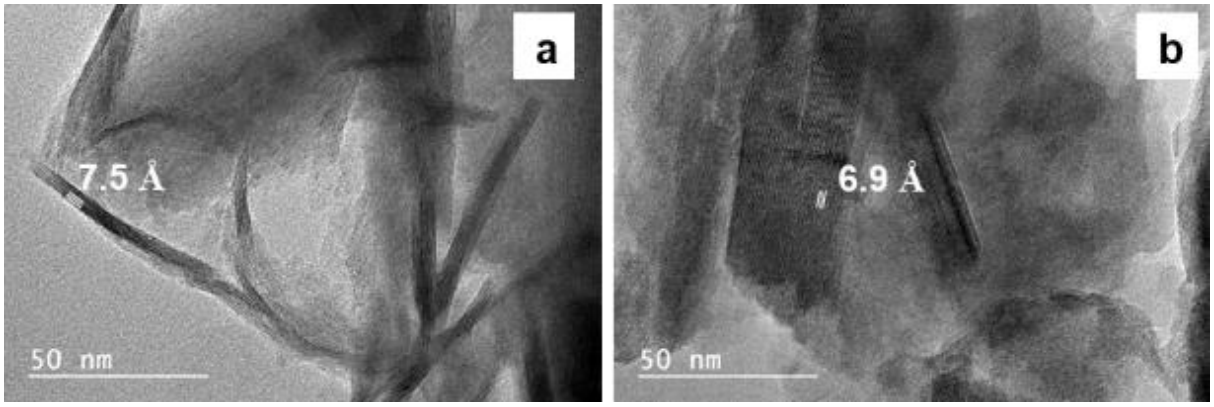

306

307 **Fig. 4.** TEM images of synthesis product with $(Fe/Si)_{ini}$ = 1.50

308 The chemical analysis revealed two sets of zones (Table 4). One with $(Fe/Si)_{EDX}$ molar ratio of
309 2.3 and the second one with $(Fe/Si)_{EDX}$ = 1.2. Both ratios were lower than determined by XRF

(Table 1). The results of XRF analysis gave the average composition for the entire synthesis product which contained different phases as shown by XRD and Mössbauer spectroscopy. However, EDX was performed over a limited zone of particles dispersed on the copper grid and, as suggested by observations, related to phyllosilicate particles.

Table 4. Semi-quantitative chemical analysis of particles of sample $(Fe/Si)_{ini}$ = 1.50 by TEM-EDX

	Set I	Set II
Element mass (%)		
O	40±1	41±1
Na	0.9±0.3	0.9±0.3
Si	10.5±0.5	17±1
Fe	48±2	41±1
Molar ratio		
$(Fe/Si)_{EDX}$	2.3±0.2	1.2±0.1

Considering the information gathered from different characterization techniques, it could be concluded that the synthetic sample contained 1:1 phyllosilicate with Fe(III) and Fe(II) entities. The $(Fe/Si)_{EDX}$ = 2.3 was close to the ratio corresponding to the crystal chemistry of cronstedtite, where Fe was located in both the octahedral (with presence of ferrous and ferric cations) and tetrahedral sheets (containing ferric cations), whereas $(Fe/Si)_{EDX}$ = 1.2 corresponded to greenalite, where Fe is located only in the octahedral sheet (only ferrous cations). Such variation of (Fe/Si) suggested important heterogeneity in the chemistry of the neoformed phyllosilicate phases.

Characterization of 2:1 Phyllosilicate Containing Synthesis Product

Powder XRD of synthesis products with $(Fe/Si)_{ini}$ from 0.50 to 1.00 were very similar and two iron-containing crystalline phases were identified: 2:1 phyllosilicate and iron oxide (Fig. 1). The analysis of the sample with $(Fe/Si)_{ini}$ = 0.75 by Mössbauer spectroscopy at room temperature showed the presence of Fe(III) only (Fig. 5). Due to the low signal/noise ratio and

the complexity of data, further analysis of Mössbauer spectra obtained at 4 K was not performed. The spectrum at room temperature permitted the hypothesis of the presence of Fe(II) in the sample to be discarded (Table 5).

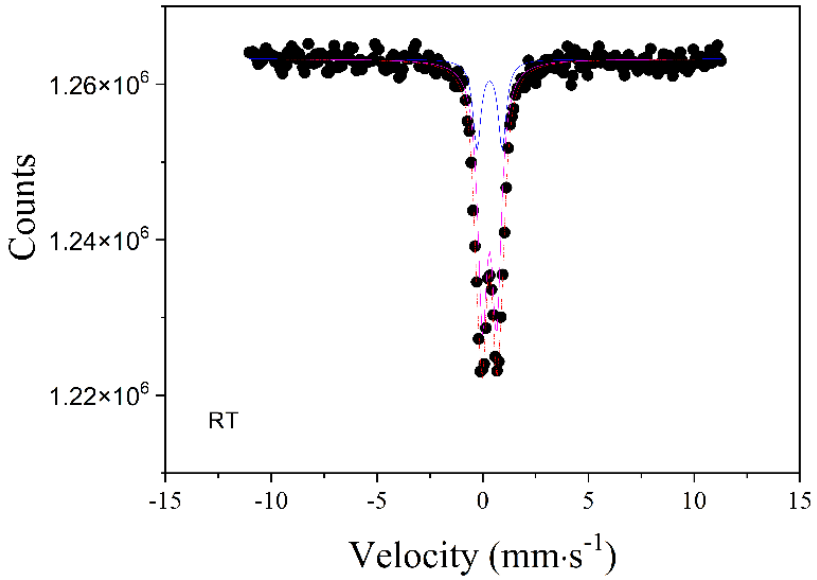

Fig. 5. Mössbauer spectrum for synthesis product with $(Fe/Si)_{ini}$ = 0.75 at 290 K

Table 5. Mössbauer parameters for synthesis product with $(Fe/Si)_{ini}$ = 0.75 at 290 K , where CS is center shift, Δ is quadrupole splitting, ε quadrupole shift, H is hyperfine field, and R.A. is relative abundance

	CS (mm/s)	Δ or ε (mm/s)	H (kOe)	R.A. (%)	
Doublet (1)	0.32	1.20		23	Fe(III) poorly cryst. iron oxides
Doublet (2)	0.32	0.67		77	Fe(III) in clay mineral

Owing to the complexity of the results from the Mössbauer spectroscopy, Raman spectroscopy was performed for this sample to investigate in more detail the possible iron oxides present in the sample (Fig. 6). Different powers were applied to examine if iron oxide would oxidize under the beam. However, the same spectral pattern was obtained, confirming that no changes happened to the sample upon its exposure to the beam. The spectrum obtained corresponded to

hematite with characteristic intense bands at 231, 290, 407, 499, 604, and 1316 cm^{-1} (Hanesch, 2009).

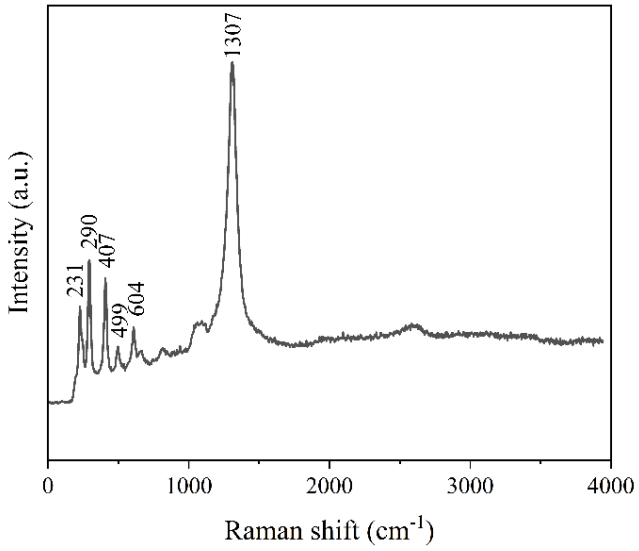

Fig. 6. Raman spectrum for synthesis product with $(Fe/Si)_{ini}$ = 0.75

In summary, Raman spectroscopy allowed the type of iron (III) oxide to be identified (not possible by XRD). This information gave a more complete vision of the complexity of the sample, where hematite was present along with 2:1 Fe(III)-rich phyllosilicate. Further characterization by XRD (oriented slides), FTIR, and TEM were undertaken to investigate in more detail the 2:1 phyllosilicate.

Regarding the 2:1 phyllosilicate, air-dried oriented preparations (AD) treated with ethylene glycol (EG) did not exhibit significant swelling, suggesting high-charge smectite or chlorite (Fig. 7). The exchange with NH_4^+ allowed the hypothesis of chlorite to be discarded; however, the asymmetry and broadness of peaks suggested a rather heterogeneous sample in terms of layer chemistry.

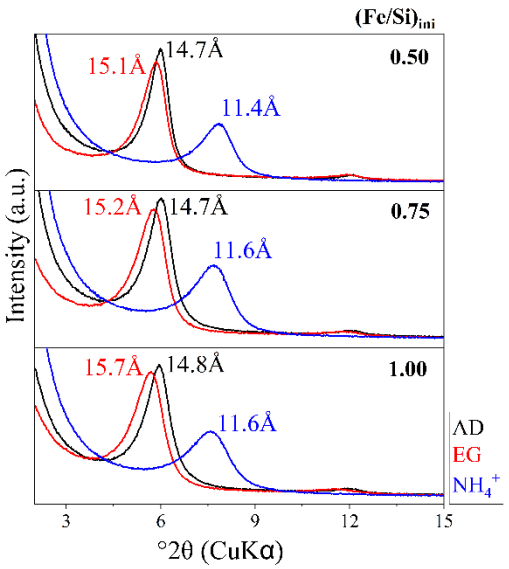

357

358 **Fig. 7.** X-ray diffractograms of oriented preparations for samples with $(Fe/Si)_{ini}$ from 0.50 to
359 1.00. AD correspond to air-dried preparation, EG – saturated with ethylene glycol and NH_4^+ –
360 exchanged with NH_4^+

361 The analysis of FTIR spectra showed characteristic O–H and Si–O vibrations (Fig. 8). The low
362 value of Si–O stretching at 980 cm^{-1} suggested Fe(III) substitution in the tetrahedral sheet
363 (Baron et al., 2016). The band of O–H stretching at 3560 cm^{-1} corresponded to the O–H group
364 linked to Fe(III). Other characteristic bands of Fe-rich smectites (nontronites) could also be
365 identified according to literature (Table 6) (Neumann et al., 2011).

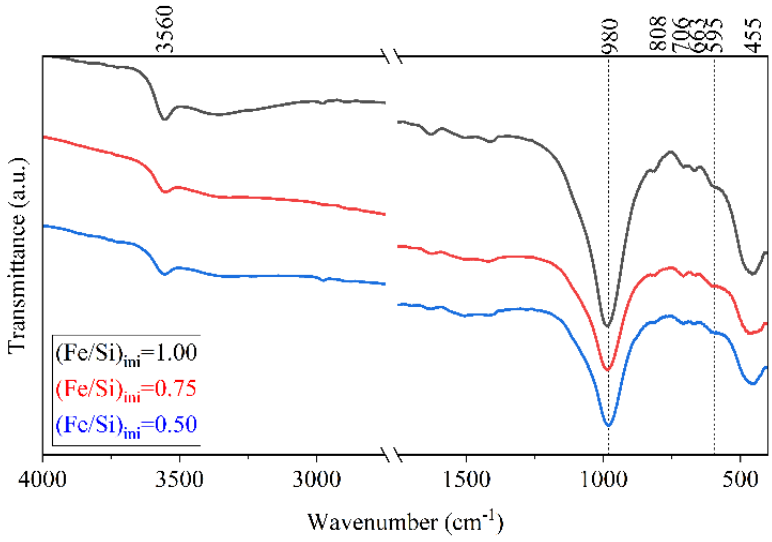

366

367 **Fig. 8.** FTIR spectra for samples with $(Fe/Si)_{ini}$ = 0.50, 0.75 and 1.00

Table 6. Identified FTIR bands and corresponding vibration modes for $(Fe/Si)_{ini}$ from 0.50 to 1.00

Wavenumber (cm^{-1})	Vibration mode
3560	O–H stretching
980	Si–O stretching
808	O–H bending
706	Fe^{3+}_{tet}–O stretching
663	Fe^{3+}_{oct}–O_{apical} out-of-plane deformation / Si-O
595	Fe^{3+}_{oct}–O_{ap}–Si^{4+}_{tet} coupled lattice deformation band
455	Si–O bending

Observation of the sample under TEM revealed the presence of platy-like particles (Fig. 9). A clear layer-type structure could be distinguished, characteristic of phyllosilicates. The measured distances between layers were in the range 11 to 12 Å, corresponding to one of 2:1 phyllosilicates. In constrast to the $(Fe/Si)_{ini}$ = 1.50 sample, all observed particles were just a few layers thick.

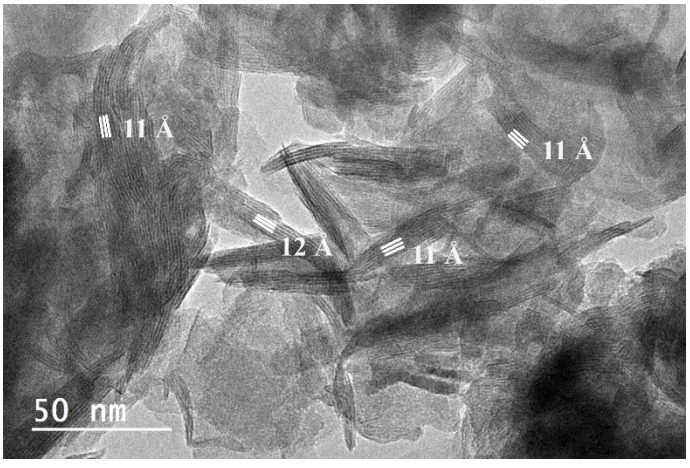

Fig. 9. TEM image of synthesis product with $(Fe/Si)_{ini}$ = 0.75

The measured chemical composition for the zones corresponding to phyllosilicates showed homogeneous distribution of elements (Table 7) contrary to two distinct zones observed previously for the sample $(Fe/Si)_{ini}$ = 1.50. The calculated average $(Fe/Si)_{EDX}$ = 1.1 ± 0.2

suggests that the average chemical composition for smectite should be $^{INT}Ca_{0.50-0.75}{}^{VI}[Fe^{3+}{}_2]^{IV}[Si_{2.5-3}Fe^{3+}{}_{1.0-1.5}]O_{10}(OH)_2$. This result is in agreement with the experiments reported by Baron et al. (2016). They reported a synthesis of high-charge nontronite with tetrahedral Fe(III) between 1.0 and 1.5 atoms per formula unit when pH > 13.

Table 7. Semi-quantitative chemical composition of sample with $(Fe/Si)_{ini} = 0.75$ determined by TEM-EDX

Element mass (%)	
O	38±1
Ca	7.2±0.3
Si	17±2
Fe	37±2
Molar ratio	
$(Fe/Si)_{EDX}$	1.1 ± 0.3

DISCUSSION

Initially, the choice was made to perform the synthesis at hydrothermal conditions in an attempt to increase the yield and crystallinity of the final synthesis product. On the one hand, this objective was reached as crystalline phyllosilicates were produced in most of the samples during synthesis. Their amount and crystallinity allowed a sufficiently detailed characterization to be carried out. On the other hand, the use of hydrothermal conditions led to processes which were difficult to control at this temperature and pressure, and which caused the experimental variables to evolve. This resulted in a rather complex mineralogy: phyllosilicates, magnetite, and/or hematite were identified in synthesis products. In addition, for the sample with $(Fe/Si)_{ini}$ = 2.33, a large decrease in pH occurred during the precipitation of the precursor and as the hydrothermal treatment "moved" this system out of the phyllosilicate stability field. The synthesis performed at lower temperatures, closer to room temperature, enabled better and continuous control of experimental conditions, and thus a precipitation of a single mineralogical

phase, as was shown in the experiments of Tosca et al. (2016) and Hinz et al. (2021). However, such an experiment requires a significantly longer time (3 months in the case of Tosca et al., 2016) or a subsequent hydrothermal treatment at higher temperatures as in the case of Hinz et al. (2021) to obtain sufficient quantities of the material for further characterization, while yield products were still very low in crystallinity.

Despite the complex mineralogy obtained, study of the phyllosilicates was still possible, as well as verifying the current hypothesis that a single phyllosilicate would form at a given initial Fe/Si. For $(Fe/Si)_{ini} < 1.50$, a 2:1 phyllosilicate, a high-charge nontronite was synthesized. Very similar samples were obtained regardless of the $(Fe/Si)_{ini}$ for this range. The formula unit found in this study was in agreement with nontronite synthesized by Baron et al. (2016) at the same pH. This suggested that in the case of nontronite the pH could be the main governing factor determining the formation of this Fe(III)-rich smectite as evidenced by Baron et al. (2016). Their results and the current study are also in agreement with previous findings (Boumaiza et al., 2020). Those authors showed that among three synthesis parameters, namely, time, temperature, and initial OH/Fe molar ratio, the last named (and consequently the pH) had the most important effect on the final synthesis product.

Another conclusion of the Boumaiza et al. (2020) study was that the kinetics of the formation of 2:1 phyllosilicate in the Fe–Si–O–H system for a given $(Fe/Si)_{ini}$ was faster compared to 1:1 phyllosilicate. As discussed already in the Introduction, this could then explain, for a given $(Fe/Si)_{ini}$, why the stoichiometry corresponds to a 2:1 phyllosilicate rather to a 1:1 phyllosilicate. Therefore, a compromise between the increase in temperature and yield, yet limiting the formation of a 2:1 phyllosilicate, must be found.

In the current study, the formation of the 1:1 phyllosilicate was achieved for $(Fe/Si)_{ini} \geq 1.50$. However, the phyllosilicate phase which formed was rather heterogeneous, showing two chemical compositions, and thus possibly two types of phases, cronstedtite and greenalite. A more rigorous control of synthesis conditions (Eh, pH) may be necessary in this particular system to synthesize a homogeneous phyllosilicate. Indeed, Pignatelli et al. (2014) presented the calculated stability fields of hematite, cronstedtite, magnetite, and greenalite, and showed that the stability field of cronstedtite at 150°C is very narrow.

In summary, the 2:1 phyllosilicate seemed to be less sensitive to redox conditions. For the 1:1 phyllosilicate, its formation also depended on pH, and also was strongly dependent on the redox conditions of the system. Indeed, Rivard et al. (2013) had shown that, in a kaolinite-iron system

under anoxic conditions, a berthierine-like phase was formed which dissolved upon introduction of O_2 into the system. It has to be noted that, even if a synthesis of homogeneous phyllosilicate could be achieved, the synthesis time was relatively short compared to the expected formation of such phyllosilicate analogues in Nature. As a consequence, synthetic iron rich phyllosilicates could be expected to be more heterogeneous than natural ones (Baker & Strawn, 2014).

Implication of the results of this study are important for engineered systems, where soluble silicon and iron species might be present. The study showed that the $(Fe/Si)_{ini} \leq 1.50$ in aqueous solution can lead to the precipitation of phyllosilicates, and thus possibly induce corrosion or scale formation. Three cases can be mentioned regarding engineered systems where such conditions might occur: (1) the scale formation in solution-conducting pipes, (2) the corrosion of steel containers or pipes, and (3) the corrosion of glass. First, regarding scale formation in solution-conducting pipes, such conditions can occur for basic solutions where the concentration of silica is high, and iron can be present such as in hyper-saline brines (Manceau et al., 1995). Such scale formation can then clog pipes and damage other equipment. Second, corrosion of the metal container or pipe can occur in an environment where such pipes or containers are surrounded by cement material. The pH of cement material is basic. As a result, some dissolved silica is expected to be present if the material is wet and porous. In contact with metal where some Fe^{2+} could be leached, the formation of phyllosilicates can then be expected, leading to further dissolution of steel. Indeed, previous studies of such a system reported the presence of phyllosilicates (Lanson et al., 2012). Third, most glass compositions contain a large amount of silica. Thus, on the glass surface a significant amount of Si–OH species can be present. In contact with steel or dissolved Fe^{2+}, phyllosilicate precipitation can then be expected due to a high Si/Fe ratio (i.e. low Fe/Si ratio). Silica consumption can then lead to glass corrosion. Indeed, the study of Carriere et al. (2021) identified phyllosilicate phases on the glass–steel interface.

CONCLUSIONS

The synthesis performed in the Fe–Si–H_2O system at 150°C showed that the initial Fe/Si molar ratio and the pH are critical parameters with regard to specificity of neoformed phases. The formation of ferrous serpentine (Fe(II)-containing) appears to be restricted to high iron concentration in solution and a very low redox range at high temperature (i.e. 150°C). In addition, a heterogeneity of formed phases (cronstedite or greenalite) was identified. For lower initial Fe/Si molar ratio, formation of a single high-charge nontronite phase was observed. The

ion exchange experiments with NH_4^+ suggested some layer heterogeneity. Thus, the hypothesis of the formation of a single one type homogeneous clay mineral was not proven. However, for lower initial Fe/Si molar ratios, one kind of mineral, nontronite, was formed. Progress is still needed to achieve better selectivity, purity, and yield for structural, chemical, and thermodynamic characterizations. The findings and study in general are of interest for engineering systems where soluble iron and silicon species might be found, in glass and steel corrosion, and scale formation in pipes.

DECLARATIONS

Funding

The study was conducted within the framework of R&D project between the French National Agency for Radioactive Waste Management (ANDRA) and CNRS.

Conflicts of interest/Competing interests

On behalf of all authors, the corresponding author states that there is no conflict of interest.

Availability of data and material

All data generated or analyzed during this study are included in this published article and its supplementary information files.

Code availability

Not applicable.

REFERENCES

Badaut, D., Besson, G., Decarreau, A., & Rautureau, R. (1985). Occurrence of a ferrous, trioctahedral smectite in recent sediments of Atlantis II Deep, Red Sea. *Clay Minerals*, *20*(3), 389–404. https://doi.org/10.1180/claymin.1985.020.3.09

Badaut, D., Decarreau, A., & Besson, G. (1992). Ferripyrophyllite and related Fe3+-rich 2:1 clays in recent deposits of Atlantis II Deep, Red Sea. *Clay Minerals*, *27*(2), 227–244. https://doi.org/10.1180/claymin.1992.027.2.07

Bailey, S. W. (1988). *Volume 19: Hydrous Phyllosilicates (Exclusive of Micas)* (S. W. Bailey (ed.)). Mineralogical Society of America.

Baker, L. L., & Strawn, D. G. (2014). Temperature effects on the crystallinity of synthetic

494 nontronite and implications for nontronite formation in Columbia river basalts. *Clays*
495 *and Clay Minerals*, *62*(2), 89–101. https://doi.org/10.1346/CCMN.2014.0620202

496 Baldermann, A., Warr, L. N., Letofsky-Papst, I., & Mavromatis, V. (2015). Substantial iron
497 sequestration during green-clay authigenesis in modern deep-sea sediments. *Nature*
498 *Geoscience*, *8*11, 885–889. https://doi.org/10.1038/ngeo2542

499 Baron, F., Petit, S., Pentrák, M., Decarreau, A., & Stucki, J. W. (2017). Revisiting the
500 nontronite Mössbauer spectra. *American Mineralogist*, *102*(7), 1501–1515.
501 https://doi.org/10.2138/am-2017-1501x

502 Baron, F., Petit, S., Tertre, E., & Decarreau, A. (2016). Influence of Aqueous Si and Fe
503 Speciation on Tetrahedral Fe(III) Substitutions in Nontronites: a Clay Synthesis
504 Approach. *Clays and Clay Minerals*, *64*(3), 230–244.
505 https://doi.org/10.1346/CCMN.2016.0640309

506 Bergaya, F, & Lagaly, G. (2013). Purification of Natural Clays. In Faïza Bergaya & G. Lagaly
507 (Eds.), *Handbook of Clay Science* (Vol. 5, pp. 213–221). Elsevier.
508 https://doi.org/10.1016/B978-0-08-098258-8.00008-0

509 Bishop, J. L., Dobrea, E. Z. N., McKeown, N. K., Parente, M., Ehlmann, B. L., Michalski, J.
510 R., Milliken, R. E., Poulet, F., Swayze, G. A., Mustard, J. F., Murchie, S. L., & Bibring,
511 J.-P. (2008). Phyllosilicate diversity and past aqueous activity revealed at Mawrth Vallis,
512 Mars. *Science*, *321*(5890), 830–833. https://doi.org/10.1126/science.1159699

513 Blanc, P., Vieillard, P., Gailhanou, H., Gaboreau, S., Gaucher, É., Fialips, C. I., Madé, B., &
514 Giffaut, E. (2015). A generalized model for predicting the thermodynamic properties of
515 clay minerals. *American Journal of Science*, *315*(8), 734 – 780.
516 https://doi.org/10.2475/08.2015.02

517 Boumaiza, H., Dutournié, P., Le Meins, J.-M., Limousy, L., Brendlé, J., Martin, C., Michau,
518 N., & Dzene, L. (2020). Iron-rich clay mineral synthesis using design of experiments
519 approach. *Applied Clay Science*, *199*, 105876.
520 https://doi.org/10.1016/j.clay.2020.105876

521 Brindley, G. W., & Brown, G. (1982). *Crystal Structures of Clay Minerals and their X-ray*
522 *Identification*. Brookfield Pub Co.

523 Carriere, C., Neff, D., Foy, E., Martin, C., Linard, Y., Michau, N., Dynes, J. J., & Dillmann,

524 P. (2017). Influence of iron corrosion on nuclear glass alteration processes: nanoscale
525 investigations of the iron-bearing phases. *Corrosion Engineering, Science and*
526 *Technology*, *52*, 166–172. https://doi.org/10.1080/1478422X.2017.1306962

527 Carriere, C., Neff, D., Martin, C., Tocino, F., Delanoë, A., Gin, S., Michau, N., Linard, Y., &
528 Dillmann, P. (2021). AVM nuclear glass/steel/claystone system altered by Callovo–
529 Oxfordian poral water with and without cement–bentonite grout at 70°C. *Materials and*
530 *Corrosion*, *72(3)*, 474–482. https://doi.org/10.1002/maco.202011766

531 Chemtob, S. M., Nickerson, R. D., Morris, R. V., Agresti, D. G., & Catalano, J. G. (2015).
532 Synthesis and structural characterization of ferrous trioctahedral smectites: Implications
533 for clay mineral genesis and detectability on Mars. *Journal of Geophysical Research:*
534 *Planets*, *120*(6), 1119–1140. https://doi.org/10.1002/2014JE004763

535 Chevrier, V., Poulet, F., & Bibring, J. (2007). Early geochemical environment of Mars as
536 determined from thermodynamics of phyllosilicates. *Nature*, *448(7149)*, 60-63.
537 https://doi.org/10.1038/nature05961

538 Chukhrov, F. V., Zvyagin, B. B., Drits, V. A., Gorshkov, A. I., Ermilova, L. P., Goilo, E. A.,
539 & Rudnitskaya, E. S. (1979). The ferric analogue of pyrophyllite and related phases. In
540 *Developments in Sedimentology* (Volume 27, pp. 55–64). https://doi.org/10.1016/S0070-
541 4571(08)70701-5

542 Decarreau, A, Bonnin, D., Badaut-Trauth, D., Couty, R., & Kaiser, P. (1987). Synthesis and
543 crystallogenesis of ferric smectite by evolution of Si-Fe coprecipitates in oxidizing
544 conditions. *Clay Minerals*, *22*(2), 207–223.
545 https://doi.org/10.1180/claymin.1987.022.2.09

546 Decarreau, A., Petit, S., Martin, F., Farges, F., Vieillard, P., & Joussein, E. (2008).
547 Hydrothermal synthesis, between 75 and 150°C, of high-charge, ferric nontronites. *Clays*
548 *and Clay Minerals*, *56*(3), 322–337. https://doi.org/10.1346/CCMN.2008.0560303

549 Ehlmann, B. L., Mustard, J. F., Murchie, S. L., Bibring, J.-P., Meunier, A., Fraeman, A. a., &
550 Langevin, Y. (2011). Subsurface water and clay mineral formation during the early
551 history of Mars. *Nature*, *479*(7371), 53–60. https://doi.org/10.1038/nature10582

552 Elmaleh, A., Bourdelle, F., Caste, F., Benzerara, K., Leroux, H., & Devouard, B. (2015).
553 Formation and transformations of Fe-rich serpentines by asteroidal aqueous alteration
554 processes: A nanoscale study of the Murray chondrite. *Geochimica et Cosmochimica*

555 *Acta*, *158*, 162–178. https://doi.org/10.1016/j.gca.2015.03.007

556 Eugster, H. P., & Chou, I.-M. (1973). The Depositional Environments of Precambrian Banded
557 Iron-Formations. *Economic Geology*, *68(7)*, 1144–1168. https://doi.org/
558 10.2113/gsecongeo.68.7.1144

559 Evans, B. W., Kuehner, S. M., Joswiak, D. J., & Cressey, G. (2017). Serpentine, iron-rich
560 phyllosilicates and fayalite produced by hydration and Mg depletion of peridotite, Duluth
561 Complex, Minnesota, USA. *Journal of Petrology*, *58*(3), 495–512.
562 https://doi.org/10.1093/petrology/egx024

563 Farmer, V. C. (1974). *The Infrared Spectra of Minerals* (V. C. Farmer (ed.)). Mineralogical
564 Society of Great Britain and Ireland. https://doi.org/10.1180/mono-4

565 Farmer, V. C., Krishnamurti, G. S. R., & Htjang, A. P. M. (1991). Synthetic allophane and
566 layer-silicate formation in SiO2-Al2O3-FeO-Fe2O3-MgO-H2O Systems at 23 and 89°C
567 in a calcareous environment. *Clays and Clay Minerals*, *39*(6), 561–570.
568 https://doi.org/10.1346/CCMN.1991.0390601

569 Fialips, C., Huo, D., Yan, L., Wu, J., & Stucki, J. W. (2002). Effect of Fe oxidation state on
570 the IR spectra of Garfield nontronite. *American Mineralogist*, *87*(5–6), 630– 641.
571 https://doi.org/10.2138/am-2002-5-605

572 Flaschen, S. S., & Osborn, E. F. (1957). Studies of the system iron oxide-silicawater at low
573 oxygen partial pressures. *Economic Geology*, *52*(8), 923–943.
574 https://doi.org/10.2113/gsecongeo.52.8.923

575 Francisco, P. C. M., Mitsui, S., Ishidera, T., Tachi, Y., Doi, R., & Shiwaku, H. (2020).
576 Interaction of FeII and Si under anoxic and reducing conditions: Structural
577 characteristics of ferrous silicate co-precipitates. *Geochimica et Cosmochimica Acta*,
578 *270*, 1–20. https://doi.org/10.1016/j.gca.2019.11.009

579 Fritz, S. J., & Toth, T. A. (1997). An Fe-berthierine from a cretaceous laterite: Part II.
580 Estimation of Eh, pH and pCO2 conditions of formation. *Clays and Clay Minerals*,
581 *45*(4), 580–586. https://doi.org/10.1346/CCMN.1997.0450409

582 Gailhanou, H., Blanc, P., Rogez, J., Mikaelian, G., Horiuchi, K., Yamamura, Y., Saito, K.,
583 Kawaji, H., Warmont, F., Grenèche, J.-M., Vieillard, P., Fialips, C. I., Giffaut, E., &
584 Gaucher, E. C. (2013). Thermodynamic properties of saponite, nontronite, and

585 vermiculite derived from calorimetric measurements. *American Mineralogist*, *98*(10),
586 1834–1847. https://doi.org/10.2138/am.2013.4344

587 Gates, W. P., Slade, P. G., Manceau, A., & Lanson, B. (2002). Site Occupancies by Iron in
588 Nontronites. *Clays and Clay Minerals*, *50*(2), 223–239.
589 https://doi.org/10.1346/000986002760832829

590 Grubb, P. L. C. (1971). Silicates and their paragenesis in the brockman iron formation of
591 Wittenoom Gorge, Western Australia. *Economic Geology*, *66*(2), 281–292.
592 https://doi.org/10.2113/gsecongeo.66.2.281

593 Hanesch, M. (2009). Raman spectroscopy of iron oxides and (oxy)hydroxides at low laser
594 power and possible applications in environmental magnetic studies. *Geophysical Journal*
595 *International*, *177*(3), 941–948. https://doi.org/10.1111/j.1365-246X.2009.04122.x

596 Harder, H. (1976). Nontronite synthesis at low temperatures. *Chemical Geology*, *18*(3), 169–
597 180. https://doi.org/10.1016/0009-2541(76)90001-2

598 Hinz, I. L., Nims, C., Theuer, S., Templeton, A. S., & Johnson, J. E. (2021). Ferric iron
599 triggers greenalite formation in simulated Archean seawater. *Geology*, *49(8)*, 905-910
600 https://doi.org/10.1130/G48495.1

601 Hybler, J. (2006). Parallel intergrowths in cronstedtite-1T: determination of the degree of
602 disorder. *European Journal of Mineralogy*, *18*(2), 197–205.
603 https://doi.org/10.1127/0935-1221/2006/0018-0197

604 Iler, R. K. (1979). *The Chemistry of Silica*. John Wiley & Sons.

605 Inoué, S., & Kogure, T. (2016). High-resolution transmission electron microscopy (HRTEM)
606 study of stacking irregularity in fe-rich chlorite from selected hydrothermal ore deposits.
607 *Clays and Clay Minerals*, *64*(2), 131–144. https://doi.org/10.1346/CCMN.2016.0640205

608 Lanson, B., Lantenois, S., van Aken, P. A., Bauer, A., & Plancon, A. (2012). Experimental
609 investigation of smectite interaction with metal iron at 80°C: Structural characterization
610 of newly formed Fe-rich phyllosilicates. *American Mineralogist*, *97*(5–6), 864–871.
611 https://doi.org/10.2138/am.2012.4062

612 Lauretta, D. S., Hua, X., & Buseck, P. R. (2000). Mineralogy of fine-grained rims in the ALH
613 81002 CM chondrite. *Geochimica et Cosmochimica Acta*, *64*(19), 3263–3273.
614 https://doi.org/10.1016/S0016-7037(00)00425-7

Le Pape, P., Rivard, C., Pelletier, M., Bihannic, I., Gley, R., Mathieu, S., Salsi, L., Migot, S., Barres, O., Villiéras, F., & Michau, N. (2015). Action of a clay suspension on an Fe(0) surface under anoxic conditions: Characterization of neoformed minerals at the Fe(0)/solution and Fe(0)/atmosphere interfaces. *Applied Geochemistry*, *61*, 62–71. https://doi.org/10.1016/j.apgeochem.2015.05.008

Manceau, A., Ildefonse, P., Hazemann, J.-L., Flank, A.-M., & Gallup, D. (1995). Crystal chemistry of hydrous iron silicate scale deposits at the Salton sea geothermal field. *Clays and Clay Minerals*, *43*(3), 304–317. https://doi.org/10.1346/CCMN.1995.0430305

Manceau, A., Lanson, B., Drits, V. A., Chateigner, D., Gates, W. P., Wu, J., Huo, D., & Stucki, J. W. (2000). Oxidation-reduction mechanism of iron in dioctahedral smectites: I. Crystal chemistry of oxidized reference nontronites. *American Mineralogist*, *85*(1), 133–152. https://doi.org/10.2138/am-2000-0114

Marcus, M. A., & Lam, P. J. (2014). Visualising Fe speciation diversity in ocean particulate samples by micro X-ray absorption near-edge spectroscopy. *Environmental Chemistry*, *11*(1), 10. https://doi.org/10.1071/EN13075

Mizutani, T., Fukushima, Y., Okada, A., Kamigaito, O., & Kobayashi, T. (1991). Synthesis of 1:1 and 2:1 iron phyllosilicates and characterization of their iron state by Mössbauer spectroscopy. *Clays and Clay Minerals*, *39*(4), 381–386. https://doi.org/10.1346/CCMN.1991.0390407

Muller, W. F., Kurat, G., & Kracher, A. (1979). Chemical and crystallographic study of cronstedtite in the matrix of the Cochabamba (CM2) carbonaceous chondrite. *TMPM Tschermaks Mineralogische Und Petrographische Mitteilungen*, *26*(4), 293–304. https://doi.org/10.1007/BF01089843

Murad, E. (2006). Chapter 12.1 Mössbauer spectroscopy of clays and clay minerals. In B. K. G. T. and G. L. B. T.-D. in C. S. Faïza Bergaya (Ed.), *Handbook of Clay Science: Vol. Volume 1* (pp. 755–764). Elsevier. https://doi.org/10.1016/S1572-4352(05)01027-5

Neumann, A., Petit, S., & Hofstetter, T. B. (2011). Evaluation of redox-active iron sites in smectites using middle and near infrared spectroscopy. *Geochimica et Cosmochimica Acta*, *75*(9), 2336–2355. https://doi.org/10.1016/j.gca.2011.02.009

Ngo, V. V, Clément, A., Michau, N., & Fritz, B. (2015). Kinetic modeling of interactions between iron, clay and water: Comparison with data from batch experiments. *Applied*

Geochemistry, *53*, 13–26. https://doi.org/10.1016/j.apgeochem.2014.12.003

Pignatelli, I, Bourdelle, F., Bartier, D., Mosser-Ruck, R., Truche, L., Mugnaioli, E., & Michau, N. (2014). Iron-clay interactions: Detailed study of the mineralogical transformation of claystone with emphasis on the formation of iron-rich T-O phyllosilicates in a step-by-step cooling experiment from 90°C to 40°C. *Chemical Geology*, *387*(1), 1–11. https://doi.org/10.1016/j.chemgeo.2014.08.010

Pignatelli, I., Mosser-Ruck, R., Mugnaioli, E., Sterpenich, J., & Gemmi, M. (2020). The effect of the starting mineralogical mixture on the nature of Fe-serpentines obtained during hydrothermal synthesis at 90°C. *Clays and Clay Minerals*, *68*(4), 394–412. https://doi.org/10.1007/s42860-020-00080-y

Rancourt, D. G., & Ping, J. Y. (1991). Voigt-based methods for arbitrary-shape static hyperfine parameter distributions in Mössbauer spectroscopy. *Nuclear Instruments and Methods in Physics Research Section B: Beam Interactions with Materials and Atoms*, *58*(1), 85–97. https://doi.org/10.1016/0168-583X(91)95681-3

Rasmussen, M. G., Evans, B. W., & Kuehner, S. M. (1998). Low-temperature fayalite, greenalite, and minnesotaite from the overlook gold deposit, Washington: Phase relations in the system FeO-SiO2-H2O. *Canadian Mineralogist*, *36*(1), 147–162.

Rivard, C., Montargès-Pelletier, E., Vantelon, D., Pelletier, M., Karunakaran, C., Michot, L. J., Villieras, F., & Michau, N. (2013). Combination of multi-scale and multi-edge X-ray spectroscopy for investigating the products obtained from the interaction between kaolinite and metallic iron in anoxic conditions at 90 °C. *Physics and Chemistry of Minerals*, *40*(2), 115–132. https://doi.org/10.1007/s00269-012-0552-6

Rivas-Sanchez, M. L., Alva-Valdivia, L. M., Arenas-Alatorre, J., Urrutia-Fucugauchi, J., Ruiz-Sandoval, M., & Ramos-Molina, M. A. (2006). Berthierine and chamosite hydrothermal: Genetic guides in the Peña Colorada magnetite-bearing ore deposit, Mexico. *Earth, Planets and Space, 58(10)*, 1389–1400. https://doi.org/10.1186/BF03352635

Roy, D. M., & Roy, R. (1954). An experimental study of the formation and properties of synthetic serpentines and related layer silicate minerals. *American Mineralogist*, *53*(11–12), 957–975.

Schlegel, M. L., Martin, C., Brucker, F., Bataillon, C., Blanc, C., Chorro, M., & Jollivet, P.

(2016). Alteration of nuclear glass in contact with iron and claystone at 90°C under anoxic conditions: Characterization of the alteration products after two years of interaction. *Applied Geochemistry*, *70*, 27–42. https://doi.org/10.1016/j.apgeochem.2016.04.009

Schulte, M., & Shock, E. (2004). Coupled organic synthesis and mineral alteration on meteorite parent bodies. *Meteoritics & Planetary Science*, *39*(9), 1577–1590. https://doi.org/10.1111/j.1945-5100.2004.tb00128.x

Stucki, J. W. (2013). Properties and behaviour of iron in clay minerals. In Faïza Bergaya & G. Lagaly (Eds.), *Handbook of Clay Science* (2nd ed., Vol. 5, Issue 1988). Elsevier Ltd. https://doi.org/10.1016/B978-0-08-098258-8.00018-3

Suquet, H., Malard, C., & Pezerat, H. (1987). Structure et proprietes d'hydratation des nontronites. *Clay Minerals*, *22*(2), 157–167. https://doi.org/10.1180/claymin.1987.022.2.04

Tardy, Y., & Garrels, R. M. (1974). A method of estimating the Gibbs energies of formation of layer silicates. *Geochimica et Cosmochimica Acta*, *38*, 1101–1116. https://doi.org/10.1016/0144-2449(86)90007-2

Tosca, N. J., Guggenheim, S., & Pufahl, P. K. (2016). An authigenic origin for Precambrian greenalite: Implications for iron formation and the chemistry of ancient seawater. *Geological Society of America Bulletin*, *128*(3–4), 511–530. https://doi.org/10.1130/B31339.1

Tutolo, B., Evans, B., & Kuehner, S. (2019). Serpentine–hisingerite solid solution in altered ferroan peridotite and olivine gabbro. *Minerals*, *9*(1), 47. https://doi.org/10.3390/min9010047

Vandenberghe, R. E., Barrero, C. A., da Costa, G. M., Van San, E., & De Grave, E. (2000). Mössbauer characterization of iron oxides and (oxy)hydroxides: the present state of the art. *Hyperfine Interactions*, *126*(1), 247–259. https://doi.org/10.1023/A:1012603603203

Vantelon, D., Montarges-Pelletier, E., Michot, L. J., Pelletier, M., Thomas, F., & Briois, V. (2003). Iron distribution in the octahedral sheet of dioctahedral smectites. An Fe K-edge X-ray absorption spectroscopy study. *Physics and Chemistry of Minerals*, *30*(1), 44–53. https://doi.org/10.1007/s00269-002-0286-y

Wilson, J. C., Benbow, S., Sasamoto, H., Savage, D., & Watson, C. (2015). Thermodynamic and fully-coupled reactive transport models of a steel–bentonite interface. *Applied Geochemistry*, *61*, 10–28. https://doi.org/10.1016/j.apgeochem.2015.05.005

Zolensky, M., Barrett, R., & Browning, L. (1993). Mineralogy and composition of matrix and chondrule rims in carbonaceous chondrites. *Geochimica et Cosmochimica Acta*, *57*(13), 3123–3148. https://doi.org/10.1016/0016-7037(93)90298-B

Zolotov, M. Y. (2014). Formation of brucite and cronstedtite-bearing mineral assemblages on Ceres. *Icarus*, *228*, 13–26. https://doi.org/10.1016/j.icarus.2013.09.020

(*Received 26 October 2021; revised 2 September 2022; AE: Jinwook Kim*)